

1 **Title:** High resolution assessment of coal mining methane emissions by satellite in Shanxi, China

2
3 **Authors**

4 Shushi Peng^{1,#,*}, Clément Giron^{2,#}, Gang Liu¹, Alexandre d'Aspremont^{2,3}, Antoine
5 Benoit², Thomas Lauvaux⁴, Xin Lin⁴, Hugo de Almeida Rodrigues², Marielle Saunois⁴,
6 Philippe Ciais^{4,5}

7
8
9 **Affiliations**

10 ¹Sino-French Institute for Earth System Science, College of Urban and Environmental
11 Sciences, and Laboratory for Earth Surface Processes, Peking University, Beijing, China.

12 ²Kayros, 33 rue Lafayette, 75009 Paris, France.

13 ³CNRS & DI, Ecole Normale Supérieure, Paris, France.

14 ⁴Laboratoire des Sciences du Climat et de l'Environnement, LSCE/IPSL, CEA-CNRS-
15 UVSQ, Université Paris-Saclay, 91191 Gif-sur-Yvette, France.

16 ⁵The Cyprus Institute 20 Konstantinou Kavafi Street, 2121, Nicosia, Cyprus.

17
18 #These authors contributed equally to this work.

19 *Correspondence to Shushi Peng (speng@pku.edu.cn)

20
21
22 This manuscript is a non-peer reviewed preprint submitted to EarthArXiv. It has been submitted
23 to a journal for peer review.

27

28 **FRONT MATTER**

29

30 **Title**

31 High resolution assessment of coal mining methane emissions by satellite in Shanxi,
32 China

33

34 **Authors**

35 Shushi Peng^{1,#,*}, Clément Giron^{2,#}, Gang Liu¹, Alexandre d'Aspremont^{2,3}, Antoine
36 Benoit², Thomas Lauvaux⁴, Xin Lin⁴, Hugo de Almeida Rodrigues², Marielle Saunois⁴,
37 Philippe Ciais^{4,5}

38

39

40 **Affiliations**

41 ¹Sino-French Institute for Earth System Science, College of Urban and Environmental
42 Sciences, and Laboratory for Earth Surface Processes, Peking University, Beijing, China.

43 ²Kayrros, 33 rue Lafayette, 75009 Paris, France.

44 ³CNRS & DI, Ecole Normale Supérieure, Paris, France.

45 ⁴Laboratoire des Sciences du Climat et de l'Environnement, LSCE/IPSL, CEA-CNRS-
46 UVSQ, Université Paris-Saclay, 91191 Gif-sur-Yvette, France.

47 ⁵The Cyprus Institute 20 Konstantinou Kavafi Street, 2121, Nicosia, Cyprus.

48

49 #These authors contributed equally to this work.

50 *Correspondence to Shushi Peng (speng@pku.edu.cn)

51

52

53 **Abstract**

54 Accurate assessment of coal mine methane (CMM) emissions is a prerequisite for defining
55 baselines and assessing the effectiveness of mitigation measures. Such an endeavor is
56 jeopardized however by large uncertainties in current CMM estimates. Here, we
57 assimilated images of methane column atmospheric mixing ratios observed by the
58 TROPOMI space borne instrument in a high-resolution regional inversion to estimate
59 CMM emissions in Shanxi, a province representing 15% of the global coal production.
60 The emissions are estimated to be 8.5 ± 0.6 and 8.6 ± 0.6 Tg CH₄ yr⁻¹ in 2019 and 2020
61 respectively, close to upper bound of current bottom-up estimates. The monthly variations
62 of emissions are well reproduced, including the drop and rebound in response to COVID-
63 19 regulation. Data from more than a thousand of individual mines indicate that our
64 estimated emission factors increase significantly with coal mining depth at prefecture
65 level, that is the CH₄ emission per volume of extracted coal. This result suggests that
66 ongoing deeper mining will increase CMM emission intensity in the future, pressing needs
67 for mitigation. Our results show robustness of estimating CMM emissions utilizing
68 TROPOMI images, and highlight potential of monitoring methane leakages and emissions
69 from satellites.

70

71 **Teaser**

72 Atmospheric methane concentration observed by TROPOMI can be applied to detect and
73 quantify coal mine methane emissions.
74

75 MAIN TEXT

76 Introduction

77 China is the world's largest anthropogenic methane (CH₄) emitter since the 2000s (1, 2).
78 Coal mining is the largest contributor, accounting for 40-45% of China's anthropogenic
79 CH₄ emissions, and ~5% of global anthropogenic emissions (3-5). During the 2000s, CH₄
80 emissions from coal mining in China increased by 12 Tg CH₄ yr⁻¹ ([6 – 18] Tg CH₄ yr⁻¹,
81 95% confidence interval) (4), contributing 85% and 32% to the increase of China's and
82 global anthropogenic CH₄ emissions, respectively (2-4). To mitigate climate change, it is
83 urgent for China to curb CH₄ emissions, especially in the coal industry. This requires a
84 solid knowledge of current emissions, including the spatial details (e.g., distribution) about
85 the most emitting areas or sites, in order to target the most effective measures and
86 prioritize mitigation actions (6).
87

88 Both bottom-up and top-down approaches give evidence for an increase in CH₄ emissions
89 from coal mining in China during the 2000s (3, 4, 7, 8). Yet, they disagree in the
90 magnitude of the trend (2, 8-10), ranging from 0.7 to 1.4 Tg CH₄ yr⁻². Furthermore, more
91 recent bottom-up inventory data shows a stabilization of coal methane emissions in the
92 2010s, mainly due to a stabilized coal production (2, 4). In contrast, recent top-down
93 estimates suggested either a significant increase in those emissions after 2010 (0.9–1.1 Tg
94 CH₄ yr⁻²) (11, 12) or a small increase (0.1–0.3 Tg CH₄ yr⁻²) (13, 14). Differences among
95 inversions could be due to the use of different prior emissions, sparse atmospheric CH₄
96 concentrations measurements from surface stations and previous satellites with coarse
97 resolution (e.g., GOSAT), making it difficult to constrain emission hotspots from coal
98 mines (4). Overall, current top-down inversion estimates of the magnitude and trend in
99 coal methane emissions in China are not consistent enough with each other to evaluate or
L00 improve bottom-up inventories.
L01

L02 The Sentinel-5P/TROPOMI (TROPOspheric Monitoring Instrument) mission, launched in
L03 2017, collects daily images of the CH₄ column mole fractions (XCH₄) at high spatial
L04 resolution (5 km × 7 km) since 2018. The TROPOMI images have been used to detect and
L05 quantify large point sources in the oil and gas production sector, including ultra-emitters
L06 (15-17), and regional extraction basins (18). Coal mine emissions from Australia have
L07 been recently examined using TROPOMI (19). Here, we focus on coal mining emissions
L08 from China, the largest coal producer of the world, and more specifically from the Shanxi
L09 Province. Shanxi represents about 15% of the global coal production, with more than 239
L10 mines producing more than 0.6 million tons of coal annually (Fig. 1). We assembled a
L11 detailed inventory data for 1,012 coal mines in the Shanxi, including mining depth, coal
L12 production and quality types, reported CH₄ ventilation/leak rates, recovery etc ... (see
L13 Methods). The Shanxi province is suitable for TROPOMI's monitoring capabilities to
L14 assess coal methane emissions using high-resolution regional inversions. We intend here
L15 to support the improvement of bottom-up inventories by not only assessing provincial
L16 total emissions, but also by identifying groups of mines with the highest emission rates.
L17
L18
L19

L20 We assimilated the TROPOMI methane column mixing ratio bias corrected level 2
L21 products in a high-resolution regional inversion to estimate CH₄ emissions from coal

production in the Shanxi province. The inversion assumes a prior map of emissions based on an annual (thus flat monthly) bottom-up inventory, with many mines but a uniform emission factor (see Methods; PKU-CH₄ v2) (4). The XCH₄ plumes generated by grid cells (0.1°×0.1°) containing at least one coal mine are simulated by the Hybrid Single-Particle Lagrangian Integrated Trajectory model (HYSPLIT) (20). Emission rates are optimized by minimizing the distance between the modeled and TROPOMI-observed XCH₄ enhancements within images for each satellite overpass (see Methods). We perform an ensemble of sensitivity tests with inversions to assess the uncertainty of posterior emissions, from TROPOMI XCH₄ measurement errors, background estimation method, meteorological data and other key parameters of the inversion (see Methods and Supplementary Text 1-2). To evaluate the impact of the prior emissions choice on posterior emissions, we also perform an inversion with no prior knowledge (Supplementary Text 3). Then we compare bottom-up inventories including EDGAR v6.0, Global Fuel Exploitation Inventory (GFEI v2) and PKU-CH₄ v2, with our independent top-down estimate derived from TROPOMI-based inversions. We further hypothesize that the CH₄ emission factor of coal mining (EF_{coal}) should be related to the depth of mining and the quality of coal that relates to different methane concentration in coal seams (21-23). Taking advantage of the fact that our inversion has a very high resolution and can distinguish between different groups of mines we finally examine the relationships between the EF_{coal} calculated from the inversion, and mining depth / coal types. This analysis provides direct insights to evaluate the bottom-up inventories emission factors.

Results

Methane emissions from large coal mines or clusters of mines produce plumes of high XCH₄, which can be detected by TROPOMI (Fig. 2A). Each large XCH₄ enhancement in the Shanxi Province is found to be associated with an ultra-emitter or a cluster of high-emitters, systematically assessed from 112 images of TROPOMI from 2019 to 2020, selecting only images with more than 30% of valid pixels (see Methods). As expected, the averaged XCH₄ enhancement map during 2019-2020 reconstructed using the optimized posterior emissions shows better agreement with the observed one ($r=0.83$, $p<0.001$) compared to the one based on the prior emissions ($r=0.42$, $p<0.001$) from the bottom-up inventory of PKU-CH₄ v2 (Fig. 2A-C). Fig. 2D shows that the (spatial) correlation coefficients between observed XCH₄ enhancements from TROPOMI images and those reconstructed from posterior emissions are higher than those modeled from prior emissions, with a mean correlation coefficient of 0.71 for posterior emissions compared to 0.31 for prior emissions across the 112 images. Moreover, the posterior emissions capture 77% of the magnitude of observed XCH₄ enhancements from the 112 TROPOMI images on average, much higher than the 51% explained by the prior emissions. In order to test the sensitivity of our inversions to meteorological data, parameters and background concentration choices for our inversions, we performed an ensemble of inversions for these uncertainties (see Methods and Supplementary Text 1-2). As a result, we found that the TROPOMI images can well constrain the methane emissions from coal mines in Shanxi with an uncertainty less than 10% (Figs. 1 and 2).

Even with an agnostic flat monthly prior, our inversion estimates based on TROPOMI (INV_{TROPOMI}) produce a seasonal variation of monthly coal production in 2019 and 2020 ($r=0.54$, $p=0.015$; Fig. 3A). Interestingly, INV_{TROPOMI} detect also a drop and rise of emissions that corresponds with the Spring Festival of 2019, and a drop of 0.1 Tg CH₄ month⁻¹ (14%) reflecting the impact of the COVID-19 outbreak on coal production, which

l71 decreased by more than 5% in February 2020. A subsequent recovery of production
l72 capacity in the next two months is also apparent in Fig. 3A. Coal mining in Shanxi emitted
l73 8.5 ± 0.6 (± 1 -sigma confidence interval) Tg CH₄ yr⁻¹ in 2019 from INV_{TROPOMI} results, and
l74 8.6 ± 0.6 Tg CH₄ yr⁻¹ in 2020 respectively (Fig. 3B). The total emissions from INV_{TROPOMI}
l75 are higher than those from PKU-CH₄ v2 (5.8 ± 0.5 Tg CH₄ yr⁻¹) and GFEI v2 (7.3 ± 2.0 Tg
l76 CH₄ year⁻¹), but similar to EDGAR v6.0 (8.8 Tg CH₄ yr⁻¹).
l77

l78 Regarding the spatial distribution of emissions inferred by INV_{TROPOMI} within Shanxi, hot-
l79 spots are detected in most grids that contain high coal production mines (Figs. 1 and 3C).
l80 However, INV_{TROPOMI} retrieves additional emission hotspots that were missing in our
l81 priori emission map (e.g., high-emissions grids in the southwest; Fig. 3). In contrast to the
l82 agnostic inversion with no prior, the spatial distribution of emissions from coal mines in
l83 EDGAR v6.0, GFEI v2 and PKU-CH₄ v2 depends on activity data such as mine locations
l84 and production and emission factors. The three bottom-up inventories have different
l85 spatial patterns, but they all miss the high-emission hotspots found by the inversion in the
l86 southwest, representing 10% of total emissions (Fig. 3D-F). We found that EDGAR v6.0,
l87 GFEI v2 and PKU-CH₄ v2 used an outdated coal production map from around 2011 to
l88 spatialize the total province-level emissions (from the product of an uniform emission
l89 factor and total coal production at province-level) into each grid cell of their emission
l90 maps (2, 24, 25). Some coal mines closed while new coal mines have opened since 2011
l91 (26), which could explain the bias in the spatial distribution of CH₄ emissions from coal
l92 mines in the bottom-up inventories, compared to INV_{TROPOMI}. The INV_{TROPOMI} optimized
l93 CH₄ emission map thus gives insights on local hotspots and how their emissions change at
l94 monthly or sub-monthly scale, although 4 out of 24 months are not covered by the
l95 inversion due to none or only one image available (fig. S1), which should be further be
l96 solved by future satellite missions (16). This method can help improving not only the total
l97 emission of the basin, but also the spatial distribution map of coal emissions, and provides
l98 timely, updated estimates to evaluate bottom-up inventories.
l99

200 Combining INV_{TROPOMI} estimate emissions at $0.1^\circ \times 0.1^\circ$ with coal production data
201 available at prefecture-level in 2019 and 2020, we deduced an inversion-based average
202 emission factor of coal methane emission (EF_{coal}) for each of the ten prefectures of Shanxi
203 (see Methods; Fig. 4). This inversion-based EF_{coal} varies by more than one order of
204 magnitude between prefectures, from $0.9 \text{ m}^3 \text{ t}^{-1}$ in Shouzhou to $17.3 \text{ m}^3 \text{ t}^{-1}$ in Yangquan.
205 Across the ten prefectures, this EF_{coal} shows marginally significant correlation with that
206 from the ground inventory ($r=0.57$, $p=0.083$; fig. S2). That inventory was conducted in
207 2011 and estimated potential fugitive emissions from underground mining without taking
208 account of coal methane utilization that already has been adopted in Shanxi (the
209 INV_{TROPOMI} assesses actual coal methane emissions including their fractional reduction
210 from methane utilization/recovery), which explains the smaller EF_{coal} in INV_{TROPOMI} (fig.
211 S2). In addition, China's energy reforms in the past decade led to the reorganization and
212 closure of some Shanxi coal mines with large emission and/or low methane utilization
213 rates (27). The large variation of EF_{coal} between prefectures highlights again that the use of
214 the same EF_{coal} for all types of mines in a region, as done in bottom-up inventories (e.g.,
215 EDGAR v6.0, PKU-CH₄ v2), could lead to strong biases in the distribution of coal CH₄
216 emissions.
217

218 The large spatial variations in EF_{coal} found between prefectures is expected to be related to
219 coal rank and mining depth (21). For example, in the northern Shanxi where the coal
220 seams in Datong, Shouzhou and Xinzhou are shallow, and mostly weakly caking coal and

221 gas coal with low metamorphic degree, we found low EF_{coal} values (Fig. 4A). On the
222 contrary, in Yangquan where the coal is mainly deep anthracite, we found the highest
223 EF_{coal} . As the degree of metamorphism of anthracite increases, methane in the interstices
224 of coal seams could decrease, which may explain the lower EF_{coal} in Shuozhou (mainly
225 gas coal) than in Yangquan (mainly anthracite).

226
227 The gas pressure of coal seam increases with depth, and so does the volume of methane
228 contained in coal. Thus, depth-specific EF_{coal} were suggested by the Intergovernmental
229 Panel on Climate Change (IPCC) methodology (28, 29), with default EF_{coal} of $10 \text{ m}^3 \text{ t}^{-1}$,
230 $18 \text{ m}^3 \text{ t}^{-1}$, and $25 \text{ m}^3 \text{ t}^{-1}$ for mines with depth less than 200m, 200-400m, and deeper than
231 400 m respectively. Among different coal ranks (coalification), a higher rank coal
232 generally has a higher methane content (23), and thus accounts for a steeper increase in
233 EF_{coal} with depth (21, 22). Almost 99% of the coal is produced from underground mines in
234 Shanxi. Mining depth shows large spatial variations from less than 100 m to more than
235 700 m (fig. S3), leading to large spatial variations in EF_{coal} . We thus regressed the EF_{coal}
236 derived from INV_{TROPOMI} against the average mining depth (from the year 2011) for each
237 prefecture, and found a high correlation ($r=0.88$, $p=0.005$) when excluding Changzhi and
238 Jinzhong prefectures which are outliers (Fig. 4B). The EF_{coal} in these two prefectures
239 could be explained by substantial subsidence of coal seams in Jinzhong and Changzhi in
240 the tectogenesis after the Carboniferous-Permian when coal was formed (e.g., depth of
241 600 m coal seam in Jinzhong similar as ~ 400 m coal seam in Changzhi or Linfen) (30,
242 31). The relationship shown in Fig. 4B suggests that EF_{coal} in these eight prefectures of
243 Shanxi increases by $9.4 \text{ m}^3 \text{ t}^{-1}$ for a 100 m increase in the mining depth. A similar
244 empirical function between coal mining depth and EF_{coal} was included in the inventory of
245 2011 across the eight prefectures ($r=0.67$, $p=0.07$; fig. S4) (22). However, at the coal mine
246 scale, this relationship could be weakened by the variability of coal ranks in different coal
247 mines (fig. S3B).

249 Discussion

250
251 To analyze the uncertainty of our posterior emissions, we performed an ensemble of tests
252 adding perturbations to the parameter values and input data (see Methods and
253 Supplementary Text 1-2). We found that the relative standard deviation of posterior
254 emissions due to errors in XCH_4 retrievals (1.4%), the uncertain release duration as
255 defined by the travel time between source locations and observed XCH_4 enhancements
256 (15%), and the uncertainty of atmospheric transport (12%) are all relatively small
257 compared to the standard deviation due to the uncertainty in background XCH_4 estimates
258 (38%, fig. S5). This suggests that the choice of background XCH_4 for calculating the
259 XCH_4 enhancement is the most important parameter to accurately estimate CH_4 emissions.
260 To test whether prior emission input affects the posterior emissions, we ran inversions
261 without any prior knowledge (zero emission for each grid in Shanxi) and used a ridge
262 regression to regularize the inverse problem (Supplementary Text 3). This sensitivity test
263 gave similar total emissions as the Bayesian inversion with prior estimates from $PKU-CH_4$
264 v2, but with lower emissions in the north and higher emissions in the middle of Shanxi
265 (figs. S6 and S7). On average, there are two to six images per month (some months have
266 11-12 images) from TROPOMI fulfilling our quality filter with $>30\%$ of valid pixels (fig.
267 S1), but for some months no image was available (e.g., June in 2019 and 2020). Future
268 satellite missions (e.g., MethaneSAT) (32) complementary with TROPOMI would help
269 better constrain the seasonal variations in emissions shown in Fig. 3A. In addition, coal

270 mines field campaigns for CMM emissions during the days when high-resolution XCH₄
271 images from satellites are available can further be used to evaluate top-down inversions in
272 the future.

273
274 Overall, we show that successive TROPOMI images of XCH₄ can constrain monthly CH₄
275 emissions from coal mining in Shanxi well, with annual emission estimates of 8.5±0.6 Tg
276 CH₄ yr⁻¹ and 8.6±0.6 Tg CH₄ yr⁻¹ in 2019 and 2020 respectively. The top-down inversion
277 with TROPOMI XCH₄ suggests that the use of a weighted average emission factor from
278 the ground inventory dataset established in 2011 underestimates CH₄ emissions from coal
279 mining (4, 25). We further find that deeper mining entails larger emission factors, as
280 shown across the prefectures in Shanxi, suggesting that emission factors are likely to
281 increase if mining deepens in the future. In addition, province-level emission factor used
282 in bottom-up inventories may smooth the spatial variation of emissions due to the
283 variation of mining depth and coal types across the mines. As the TROPOMI-based
284 inversion used in our study can capture seasonal variation of coal mining activity
285 (especially the drop in emissions corresponding to the coal production decrease in
286 February, 2020 after the outbreak of COVID-19), a near real-time emission map can be
287 updated on a regular basis. Such a tool could help monitoring and verification of
288 emissions as well as supporting mitigation toward climate neutrality targets.

289 **Materials and Methods**

291 **Satellite-based XCH₄ retrievals from TROPOMI**

292 We collected bias-corrected methane column mixing ratios derived from the spaceborne
293 instrument TROPOMI on board of the Sentinel 5P satellite (ESA products of S5P L2 CH₄
294 OFFLINE) (33). TROPOMI is an imaging spectrometer, orbiting the earth in near-polar,
295 sun-synchronous trajectories with a mean local solar time ascending node at 13:30.
296 TROPOMI's swath is approximately 2600 km wide, achieving near-global coverage on a
297 daily basis. Our study relies on TROPOMI measurements from January 2019 to December
298 2020, with images collected over the Shanxi Province shape, and re-projected on a
299 0.1°×0.1° regular grid using the GDAL library (34). As cloud cover, high solar zenith
300 angle, high viewing zenith angle, large terrain roughness or small surface albedo etc.
301 induce substantial bias in XCH₄ retrievals (33), we only used pixels with a quality
302 assurance value (qa_value = 1). TROPOMI images were filtered to keep only those with
303 more than 30% of valid pixels (qa_value = 1). With this filter, 58 and 54 images were
304 selected per year in 2019 and 2020 respectively. Uneven albedo and aerosol optical
305 thickness are amongst the parameters influencing the quality and accuracy of TROPOMI
306 XCH₄ retrievals. Although the data product we used in this study includes a correction
307 based on surface albedo in the SWIR domain (35), we also assessed the reliability of
308 TROPOMI XCH₄ retrievals by evaluating its correlation with surface shortwave infrared
309 albedo (Albedo) and aerosols optical thickness (AOD) (fig. S8). When using only high-
310 quality pixels (qa_value = 1), R² scores of linear regressions between bias-corrected XCH₄
311 and Albedo (R²=0.010) and AOD (R²=0.006) are quite low, hence significant bias of
312 XCH₄ from albedo or aerosols can be dismissed. When including medium-quality pixels
313 (qa_value ≥ 0.4), the R² scores are estimated respectively at 0.007 and 0.130 for albedo
314 and AOD, confirming that the albedo and aerosols has limited impact on XCH₄ retrievals
315 in our region of interest.

317 **Bottom-up inventories for coal CH₄ emissions**

Three bottom-up inventories for annual methane emissions from coal mining in the Shanxi province were used in this study: PKU-CH₄ v2 (4), EDGAR v6.0 (2) and GFEI v2 (24). PKU-CH₄ v2 was updated up to 2020 using annual coal production in 2020 from the latest Statistic Yearbook, following the bottom-up methodology in Liu et al. (2021) (4). The annual maps from PKU-CH₄ v2 were used as prior for our top-down inversion. For the EDGAR v6.0, we used the monthly gridded emissions of China in 2018, and then calculated the total emission as the sum of all grids in Shanxi province. We then scaled the emissions in 2018 from EDGAR v6.0 into emissions in 2019 by using the ratio of coal production of Shanxi in 2019 and 2018. This estimate is referred as EDGAR v6.0. The inventory of GFEI v2 gives the annual emissions that incorporate national reports of China to the United Nations Framework Convention on Climate Change (UNFCCC) and allocates the total national emissions into infrastructure locations from Sheng et al. (2019) (25) with a 0.1°×0.1° spatial resolution (24). We used annual emissions of 2019 from GFEI v2 here, updated with IPCC emission factors and yearly activity data from US Energy Information Administration (24, 36). To validate seasonal variation of top-down monthly emissions, the monthly coal production of Shanxi province and yearly coal production in prefecture level were collected from Shanxi Statistic Yearbook (37).

Ground inventory from 1012 coal mines in 2011

We collected the information of coal mines in Shanxi province publicly available in the ground inventory of the National Coal Mine Methane Level Identification for 2011, by the State Administration of Coal Mine Safety (38). The coal production in Shanxi province increased by ~60% from 2011 to 2020. Emission factors from this inventory have been applied to estimate CH₄ emissions from coal mining in Sheng et al. (2019) (25) and Liu et al. (2021) (4). We collected data from 1012 coal mines, more than 95% coal mines in Shanxi province, including annual coal production (537 coal mines), mining depth (984 coal mines) and emission factors (727 coal mines) reported in the ground inventory of 2011. The location of these coal mines were derived from Baidu Map Platform (<http://api.map.baidu.com/lbsapi/getpoint/index.html>). Note that 84 out of the 1012 coal mines are excluded in our analysis, as these 84 coal mines have been closed since 2016 because of a supply-side structural reform of the coal industry by eliminating low efficiency coal production (27).

According to the ground inventory and the locations of coal mines, we aggregate the production and average the mining depth, extraction rate and emission factors weighted by the coal production into 0.1°×0.1° grid scale in 2011. For the map of coal production in 2019 (2020), we scaled the map of 2011 by the ratio of total province-level production in 2019 (2020) and in 2011. The main types of coal for each prefecture in Shanxi were collected from the dataset in Liu et al. (2015) (39). To compare the EF_{coal} derived from INV_{TROPOMI} in 2019, we adjusted the EF_{coal} derived from ground inventory in 2011 by the composition of coal production mined from low gas mines, high gas mines and outburst gas mines in each prefecture between 2019 and 2011 in fig. S3.

TROPOMI-based top-down inversion

Model

The estimates are produced using a classical Bayesian regression framework (40, 41). Specifically, we solve the following quadratic programming problem for each useable TROPOMI XCH₄ image

$$\begin{aligned} \min_x \quad & J(x) = (y - Kx)^T S_o^{-1} (y - Kx) + \lambda (x - x_p)^T S_p^{-1} (x - x_p) \\ \text{s.t.} \quad & x \geq 0 \end{aligned}$$

where y is the methane column mixing ratio enhancement (i.e. methane column mixing ratio bias corrected image subtracted from its median value and with negative values clipped to 0); K is the methane dispersion footprints produced using the Hybrid Single-Particle Lagrangian Integrated Trajectory model (HYSPLIT) (20); x_p is the prior emission rates vector (all $0.1^\circ \times 0.1^\circ$ regular grid cells); S_o is the covariance matrix for observational error; S_p is the covariance matrix for prior error (40, 42).

If we omit the non-negativity constraint $x \geq 0$, this quadratic program can be solved in closed form by

$$x = x_p + \lambda^{-1} S_p K^T (\lambda^{-1} K S_p K^T + S_o)^{-1} (y - K x_p)$$

and a condition number of this problem can be computed to assess the stability and

robustness of the solution. This condition number is defined as $\kappa(\lambda) = \frac{\sigma_{max}(\tilde{S}_\lambda)}{\sigma_{min}(\tilde{S}_\lambda)}$ with

σ_{max} (resp. σ_{min}) denoting the highest (resp. smallest) singular value of $\tilde{S}_\lambda = (K^T S_o^{-1} K + \lambda S_p^{-1})^{-1}$. We add the non-negativity constraint for x and solve the quadratic program numerically. This constraint regularizes the solution and limits overfit. λ is used to scale the relative weights of the TROPOMI XCH4 image and prior terms. It should ideally be equal to 0 or very small. Yet for several dates, the quadratic program is ill-conditioned due to the sparsity of the TROPOMI XCH4 image and near-colinearity of some HySplit footprints ($\kappa(\lambda) \gg 0$). We ensure that the estimates for each date are produced by a well-conditioned minimization program by incrementing $\lambda \in [10^{-2}, 10^2]$ on a \log_{10} scale up to the smallest value such that $\kappa(\lambda) < \tau$. We set $\tau = 10^3$ based on the criterions explained in Supplementary Text 1.

Observational and prior error covariance matrices

S_o is computed using the relative residual error method (42). In particular, we split our work domain into a $2^\circ \times 2^\circ$ grid and compute the standard deviation matrix of the residual error in the bias corrected subtraction of observed methane concentrations by simulated concentrations (derived from HySplit simulations and prior PKU-CH₄ v2 emission rates). S_o is defined as the normalized, relative standard deviation matrix and, by construction, it accounts for both the sensor error and the model error. S_p is defined as the absolute error between the gridded inventories PKU-CH₄ v2 and EDGAR v6.0, re-projected on the same $0.1^\circ \times 0.1^\circ$ regular grid as the images. Both S_o and S_p are normalized so that their relative weight in the objective function J is fully controlled by the parameter λ . In addition, very small diagonal values of S_p are set at 1/10 of its maximal value (i.e. 0.1 after minmax normalization) to avoid ill-conditioning that would occur when EDGAR v6.0 and PKU-CH₄ v2 have very similar values. In more than 97% of the daily inversions, the condition number criterion yields $\lambda \in \{10^{-2}, 10^{-1}, 1\}$, hence giving to the observational term a greater or equal weight with respect to the prior penalization term.

HySplit simulations

Each grid pixel with a positive methane emissions value in the PKU-CH₄ v2 inventory is considered as a potential source from which we simulate methane plumes using the Lagrangian particle dispersion model HySplit. These simulations are executed in concentration, forward mode on a $0.01^\circ \times 0.01^\circ$ grid and re-projected on the priors and images $0.1^\circ \times 0.1^\circ$ grid. HySplit parameters are mostly similar to those used in Lauvaux et al. (2022) (16). Particles are released continuously at constant rate (10000 particles per hour) from a grid cell; each particle represents a fixed amount of methane spreading horizontally as a gaussian puff with respect to the meteorological fields. The Planetary Boundary Layer in which the particles diffuse vertically is derived from the meteorological data. The release altitude is set at 10 meters, consistent with the fact that

methane is mainly emitted from coal mines through Ventilation Air Methane (VAM) devices located close to the ground level. Following the analysis of Lauvaux et al. (2022) (16) on the negligible impact of the parameters defining the mixed layer height model and vertical mixing strength, we keep these parameters at default value. These fields come from the Global Data Assimilation System (GDAS) meteorological data produced by the National Centers for Environmental Prediction (NCEP) at 1-degree spatial resolution and sampled hourly; they are downloaded from the NOAA FTP server. For sensitivity analysis purposes, we also rely on data from the Global Forecast System (GFS), also produced by NCEP at $0.25^\circ \times 0.25^\circ$ spatial and hourly temporal resolutions available on the same NOAA FTP server.

Release is set to start 10 hours before TROPOMI overpass time, assuming that the simulated plumes have reached a steady state at sensing time. This hypothesis is discussed and supported in Supplementary Text 2. HySplit plumes thereby obtained are normalised to produce footprints which play the same role as the Jacobian matrix derived from GEOS-FP data in Zhang et al. (2020) (40), Shen et al. (2021) (41).

Uncertainty

Uncertainty in the methane emission estimate stems from several parameters, modelling choices and data-induced constraints. To account for the modelling uncertainty, we perform an ensemble of inversion with perturbations of the parameters and input data. Notably, we evaluate the standard deviation of the methane emission estimates with respect to variations in meteorological data, simulation duration and methane background estimation process, respectively denoted σ_w , σ_d , σ_b . More details on the ensemble sensitivity analysis are given in Supplementary Text 2. We also propagate the TROPOMI error, as provided by the *precision* data product (43), to derive the sensor measurement error σ_m . We also account for the absence of valid readings for some days (namely sampling uncertainty σ_s) by using a poll setting and deriving σ_s from the unbiased Horvitz-Thompson confidence bounds (see paragraph S2) (44). Assuming independence of the uncertainty sources, we finally apply the law of propagation of uncertainty to evaluate the total uncertainty $\sigma = \sqrt{\sigma_w + \sigma_d + \sigma_b + \sigma_m + \sigma_s}$.

The condition numbers and the degrees of freedom for signal (DOFS; defined as $\text{trace}(I - \tilde{S}_\lambda S_p^{-1})$ where I is the identity matrix) of the quadratic programs solved in the inversions are qualitative indicators for the sensitivity of the results produced. These are discussed in the next section.

Validation

To assess the validity and robustness of the results, we compute a series of metrics and indicators. This includes the distribution of correlations between observed TROPOMI images and prior and posterior reconstructed images (Fig. 2); the correlation between the mean observed image and the mean reconstructed images (Fig. 2D); and the percentage of reconstructed methane with respect to observed images (Fig. 2E). On average, the mean image-per-image correlation increases from 0.31 (prior reconstruction) to 0.71 (posterior reconstruction) after the optimization process. The same metrics on averaged images rises from 0.42 to 0.83, hence validating the ability of the model to explain local methane enhancements by emissions originating in coal mining areas. The mean posterior percentage of methane reconstructed is 76%, thus indicating that a minor part of the observed methane enhancements is not explained by coal mining emissions.

165 The condition number criterion is discussed and supported in Supplementary Text 1 (Figs.
166 S9 and S10). In particular, we show that this criterion leads to λ parameters mostly
167 comprised in $\{10^{-2}, 10^{-1}, 1\}$, hence efficiently improving the conditioning of the
168 quadratic programs without over-penalizing the objective function (which would
169 artificially lower the emissions estimates). Likewise, the distribution of the DOFS of the
170 system has a lower bound at 20 with a mean value at 75. It shows that the quadratic
171 programs are well-constrained, namely that output of the optimization problem is largely
172 influenced by TROPOMI images and not primarily determined by the prior term (fig.
173 S10).

174 Figures 2 and 3 reveal a high stability in the estimates, both monthly and hourly,
175 aggregated and on a gridded basis (standard deviation of the monthly estimates is 0.11Mt).
176 This is expected as ventilation air methane systems are set to continuously ventilate coal
177 mines, and it argues for the robustness of the inversion estimates.

178 We show that the results have a very low sensitivity to the construction of the
179 minimization problem. A pure ridge regression setting ($S_O = I_n$, $S_p = I_n$ and $x_p = 0$)
180 produces very similar methane emission estimates and validation metrics (see
181 Supplementary Text 3 and figs. S6 and S7).

184 References

- 185 1. National Development and Reform Commission of the People's Republic of China. Second
186 National Communication on Climate Change of The People's Republic of China. (UNFCCC,
187 2012).
- 188 2. Crippa, M., Guizzardi, D., Solazzo, E., Muntean, M., Schaaf, E., Monforti-Ferrario, F., Banja,
189 M., Olivier, J.G.J., Grassi, G., Rossi, S., Vignati, E. GHG emissions of all world countries -
190 2021 Report, EUR 30831 EN, Publications Office of the European Union, Luxembourg, 2021,
191 ISBN 978-92-76-41547-3, JRC126363.
- 192 3. S. Peng, S. Piao, P. Bousquet, P. Ciais, B. Li, X. Lin, S. Tao, Z. Wang, Y. Zhang, F. Zhou,
193 Inventory of anthropogenic methane emissions in Mainland China from 1980 to 2010.
194 Atmospheric Chemistry and Physics Discussions, 1-29 (2016).
- 195 4. G. Liu, S. Peng, X. Lin, P. Ciais, X. Li, Y. Xi, Z. Lu, J. Chang, M. Saunois, Y. Wu, P. Patra,
196 N. Chandra, H. Zeng, S. Piao, Recent Slowdown of Anthropogenic Methane Emissions in
197 China Driven by Stabilized Coal Production. Environmental Science & Technology Letters 8,
198 739-746 (2021).
- 199 5. M. Saunois, A. R. Stavert, B. Poulter, P. Bousquet, J. G. Canadell, R. B. Jackson, P. A.
500 Raymond, E. J. Dlugokencky, S. Houweling, P. K. Patra, P. Ciais, V. K. Arora, D. Bastviken,
501 P. Bergamaschi, D. R. Blake, G. Brailsford, L. Bruhwiler, K. M. Carlson, M. Carrol, S.
502 Castaldi, N. Chandra, C. Crevoisier, P. M. Crill, K. Covey, C. L. Curry, G. Etiope, C.
503 Frankenberg, N. Gedney, M. I. Hegglin, L. Höglund-Isaksson, G. Hugelius, M. Ishizawa, A.
504 Ito, G. Janssens-Maenhout, K. M. Jensen, F. Joos, T. Kleinen, P. B. Krummel, R. L.
505 Langenfelds, G. G. Laruelle, L. Liu, T. Machida, S. Maksyutov, K. C. McDonald, J.
506 McNorton, P. A. Miller, J. R. Melton, I. Morino, J. Müller, F. Murguia-Flores, V. Naik, Y.
507 Niwa, S. Noce, S. O'Doherty, R. J. Parker, C. Peng, S. Peng, G. P. Peters, C. Prigent, R. Prinn,
508 M. Ramonet, P. Regnier, W. J. Riley, J. A. Rosentreter, A. Segers, I. J. Simpson, H. Shi, S. J.
509 Smith, L. P. Steele, B. F. Thornton, H. Tian, Y. Tohjima, F. N. Tubiello, A. Tsuruta, N.
510 Viovy, A. Voulgarakis, T. S. Weber, M. van Weele, G. R. van der Werf, R. F. Weiss, D.
511 Worthy, D. Wunch, Y. Yin, Y. Yoshida, W. Zhang, Z. Zhang, Y. Zhao, B. Zheng, Q. Zhu, Q.

- 512 Zhu, Q. Zhuang, The Global Methane Budget 2000–2017. *Earth Syst. Sci. Data* 12, 1561-
513 1623 (2020).
- 514 6. Y. Y. Lu, H. D. Zhang, Z. Zhou, Z. L. Ge, C. J. Chen, Y. D. Hou, M. L. Ye, Current Status
515 and Effective Suggestions for Efficient Exploitation of Coalbed Methane in China: A Review.
516 *Energy & Fuels* 35, 9102-9123 (2021).
- 517 7. P. Bergamaschi, S. Houweling, A. Segers, M. Krol, C. Frankenberg, R. A. Scheepmaker, E.
518 Dlugokencky, S. C. Wofsy, E. A. Kort, C. Sweeney, T. Schuck, C. Brenninkmeijer, H. Chen,
519 V. Beck, C. Gerbig, Atmospheric CH₄ in the first decade of the 21st century: Inverse
520 modeling analysis using SCIAMACHY satellite retrievals and NOAA surface measurements.
521 *Journal of Geophysical Research: Atmospheres* 118, 7350-7369 (2013).
- 522 8. R. L. Thompson, A. Stohl, L. X. Zhou, E. Dlugokencky, Y. Fukuyama, Y. Tohjima, S.-Y.
523 Kim, H. Lee, E. G. Nisbet, R. E. Fisher, D. Lowry, R. F. Weiss, R. G. Prinn, S. O'Doherty, D.
524 Young, J. W. C. White, Methane emissions in East Asia for 2000–2011 estimated using an
525 atmospheric Bayesian inversion. *Journal of Geophysical Research: Atmospheres* 120, 4352-
526 4369 (2015).
- 527 9. US EPA (US Environmental Protection Agency): Global Anthropogenic Non-CO₂ Greenhouse
528 Gas Emissions: 1990-2030, (United States Environmental Protection Agency, 2012).
- 529 10. J. Gao, C. Guan, B. Zhang, China's CH₄ emissions from coal mining: A review of current
530 bottom-up inventories. *Science of The Total Environment* 725, 138295 (2020).
- 531 11. S. M. Miller, A. M. Michalak, R. G. Detmers, O. P. Hasekamp, L. M. P. Bruhwiler, S.
532 Schwietzke, China's coal mine methane regulations have not curbed growing emissions.
533 *Nature Communications* 10, 303 (2019).
- 534 12. Y. Yin, F. Chevallier, P. Ciais, P. Bousquet, M. Saunois, B. Zheng, J. Worden, A. A. Bloom,
535 R. J. Parker, D. J. Jacob, E. J. Dlugokencky, C. Frankenberg, Accelerating methane growth
536 rate from 2010 to 2017: leading contributions from the tropics and East Asia. *Atmos. Chem.*
537 *Phys.* 21, 12631-12647 (2021).
- 538 13. Y. Zhang, D. J. Jacob, X. Lu, J. D. Maasackers, T. R. Scarpelli, J. X. Sheng, L. Shen, Z. Qu,
539 M. P. Sulprizio, J. Chang, A. A. Bloom, S. Ma, J. Worden, R. J. Parker, H. Boesch,
540 Attribution of the accelerating increase in atmospheric methane during 2010–2018 by inverse
541 analysis of GOSAT observations. *Atmos. Chem. Phys.* 21, 3643-3666 (2021).
- 542 14. X. Lu, D. J. Jacob, Y. Zhang, J. D. Maasackers, M. P. Sulprizio, L. Shen, Z. Qu, T. R.
543 Scarpelli, H. Nesser, R. M. Yantosca, J. Sheng, A. Andrews, R. J. Parker, H. Boesch, A. A.
544 Bloom, S. Ma, Global methane budget and trend, 2010–2017: complementarity of inverse
545 analyses using in situ (GLOBALVIEWplus CH₄ ObsPack) and satellite (GOSAT)
546 observations. *Atmos. Chem. Phys.* 21, 4637-4657 (2021).
- 547 15. D. J. Varon, J. McKeever, D. Jervis, J. D. Maasackers, S. Pandey, S. Houweling, I. Aben, T.
548 Scarpelli, D. J. Jacob, Satellite Discovery of Anomalously Large Methane Point Sources From
549 Oil/Gas Production. *Geophysical Research Letters* 46, 13507-13516 (2019).
- 550 16. T. Lauvaux, C. Giron, M. Mazzolini, A. d'Aspremont, R. Duren, D. Cusworth, D. Shindell, P.
551 Ciais, Global assessment of oil and gas methane ultra-emitters. *Science* 375, 557-561 (2022).
- 552 17. I. Irakulis-Loitxate, L. Guanter, Y.-N. Liu, D. J. Varon, J. D. Maasackers, Y. Zhang, A.
553 Chulakadabba, S. C. Wofsy, A. K. Thorpe, R. M. Duren, C. Frankenberg, D. R. Lyon, B.
554 Hmiel, D. H. Cusworth, Y. Zhang, K. Segl, J. Gorroño, E. Sánchez-García, M. P. Sulprizio,
555 K. Cao, H. Zhu, J. Liang, X. Li, I. Aben, D. J. Jacob, Satellite-based survey of extreme
556 methane emissions in the Permian basin. *Science Advances* 7, eabf4507 (2021).

- 557 18. Z. Deng, P. Ciais, Z. A. Tzompa-Sosa, M. Saunio, C. Qiu, C. Tan, T. Sun, P. Ke, Y. Cui, K.
558 Tanaka, X. Lin, R. L. Thompson, H. Tian, Y. Yao, Y. Huang, R. Lauerwald, A. K. Jain, X.
559 Xu, A. Bastos, S. Sitch, P. I. Palmer, T. Lauvaux, A. d'Aspremont, C. Giron, A. Benoit, B.
560 Poulter, J. Chang, A. M. R. Petrescu, S. J. Davis, Z. Liu, G. Grassi, C. Albergel, F. N.
561 Tubiello, L. Perugini, W. Peters, F. Chevallier, Comparing national greenhouse gas budgets
562 reported in UNFCCC inventories against atmospheric inversions. *Earth Syst. Sci. Data* 14,
563 1639-1675 (2022).
- 564 19. P. Sadavarte, S. Pandey, J. D. Maasackers, A. Lorente, T. Borsdorff, H. Denier van der Gon,
565 S. Houweling, I. Aben, Methane Emissions from Superemitting Coal Mines in Australia
566 Quantified Using TROPOMI Satellite Observations. *Environmental Science & Technology*
567 55, 16573-16580 (2021).
- 568 20. A. F. Stein, R. R. Draxler, G. D. Rolph, B. J. B. Stunder, M. D. Cohen, F. Ngan, NOAA's
569 HYSPLIT Atmospheric Transport and Dispersion Modeling System. *Bulletin of the American*
570 *Meteorological Society* 96, 2059-2077 (2015).
- 571 21. N. Kholod, M. Evans, R. C. Pilcher, V. Roshchanka, F. Ruiz, M. Coté, R. Collings, Global
572 methane emissions from coal mining to continue growing even with declining coal
573 production. *Journal of Cleaner Production* 256, 120489 (2020).
- 574 22. Z. Wang, X. Wang, W. Zuo, X. Ma, N. Li, The influence of temperature on methane
575 adsorption in coal: A review and statistical analysis. *Adsorption Science & Technology* 37,
576 745-763 (2019).
- 577 23. Z. Zhou, F. Shi, Y. Zhang, Y. Yu, S. Tang, in *Communications, Signal Processing, and*
578 *Systems*, Q. Liang, W. Wang, X. Liu, Z. Na, X. Li, B. Zhang, Eds. (Springer Singapore,
579 Singapore, 2021), pp. 278-284.
- 580 24. T. R. Scarpelli, D. J. Jacob, S. Grossman, X. Lu, Z. Qu, M. P. Sulprizio, Y. Zhang, F.
581 Reuland, D. Gordon, J. R. Worden, *x Atmos. Chem. Phys.* 22, 3235-3249 (2022).
- 582 25. J. Sheng, S. Song, Y. Zhang, R. G. Prinn, G. Janssens-Maenhout, Bottom-Up Estimates of
583 Coal Mine Methane Emissions in China: A Gridded Inventory, Emission Factors, and Trends.
584 *Environmental Science & Technology Letters* 6, 473-478 (2019).
- 585 26. National Energy Administration of the People's Republic of China (NEA). Shanxi plans to
586 add 100 million tons of coal production capacity, 2013. Available at:
587 http://www.nea.gov.cn/2013-05/03/c_132357516.htm (in Chinese).
- 588 27. P. Lu, L. Zhou, S. Cheng, X. Zhu, T. Yuan, D. Chen, Q. Feng, Main challenges of
589 closed/abandoned coal mine resource utilization in China. *Energy Sources, Part A: Recovery,*
590 *Utilization, and Environmental Effects* 42, 2822-2830 (2020).
- 591 28. IPCC in *Climate Change 2013: The Physical Science Basis. Contribution of Working Group I*
592 *to the Fifth Assessment Report of the Intergovernmental Panel on Climate Change*, T. F.
593 Stocker et al., Eds. (Cambridge Univ. Press, New York, 2013)
- 594 29. IPCC in 2019 Refinement to the 2006 IPCC Guidelines for National Greenhouse Gas
595 Inventories (available at: [https://www.ipcc.ch/report/2019-refinement-to-the-2006-ipcc-](https://www.ipcc.ch/report/2019-refinement-to-the-2006-ipcc-guidelines-for-national-greenhouse-gas-inventories/)
596 [guidelines-for-national-greenhouse-gas-inventories/](https://www.ipcc.ch/report/2019-refinement-to-the-2006-ipcc-guidelines-for-national-greenhouse-gas-inventories/), 2019)
- 597 30. L. Sun, X. Jin, C. Wen, P. Bian, The Structure and Seismic Activity Characteristics of Jinhua
598 Fault Zone. *NORTH CHINA EARTHQUAKE SCIENCES* 27, (2009) (in Chinese).
- 599 31. K. Liu, D. Cao, Z. Lin, J. Li, Subsidence history of central-northern Qinshui basin. *COAL*
600 *GEOLOGY & EXPLORATION* 41, (2013) (in Chinese).

32. D. J. Jacob, D. J. Varon, D. H. Cusworth, P. E. Dennison, C. Frankenberg, R. Gautam, L. Guanter, J. Kelley, J. McKeever, L. E. Ott, B. Poulter, Z. Qu, A. K. Thorpe, J. R. Worden, R. M. Duren, Quantifying methane emissions from the global scale down to point sources using satellite observations of atmospheric methane. *Atmos. Chem. Phys. Discuss.* 2022, 1-44 (2022).
33. ESA, S5P Mission Performance Centre Methane [L2__CH4__] Readme. V01.04.00 (2020).
34. GDAL/OGR contributors. Geospatial Data Abstraction Software Library. <https://gdal.org> (2021).
35. Hasekamp, O.; Lorente, A.; Hu, H.; Butz, A.; Aan de Brugh, J.; Landgraf, J., Algorithm Theoretical Baseline Document for Sentinel-5 Precursor Methane Retrieval. SRON-S5P-LEV2-RP-001, CI-7430-ATBD, Issue 2.3.1. (2021).
36. EIA: International Energy Statistics (EIA, 2021); <https://www.eia.gov/international/data/world>.
37. Shanxi Statistical Yearbook. (China Statistics Press, Beijing, 2020)
38. State Administration of Coal Mine Safety (SACMS). Compilation of National Coal Mine Gas Level Identification for 2011. (National Mine Safety Administration Press, Beijing, 2012)
39. Z. Liu, D. Guan, W. Wei, S. J. Davis, P. Ciaus, J. Bai, S. Peng, Q. Zhang, K. Hubacek, G. Marland, R. J. Andres, D. Crawford-Brown, J. Lin, H. Zhao, C. Hong, T. A. Boden, K. Feng, G. P. Peters, F. Xi, J. Liu, Y. Li, Y. Zhao, N. Zeng, K. He, Reduced carbon emission estimates from fossil fuel combustion and cement production in China. *Nature* 524, 335-338 (2015).
40. Y. Zhang, R. Gautam, S. Pandey, M. Omara, J. D. Maasackers, P. Sadavarte, D. Lyon, H. Nesser, M. P. Sulprizio, D. J. Varon, R. Zhang, S. Houweling, D. Zavala-Araiza, R. A. Alvarez, A. Lorente, S. P. Hamburg, I. Aben, D. J. Jacob, Quantifying methane emissions from the largest oil-producing basin in the United States from space. *Science Advances* 6, eaaz5120 (2020).
41. L. Shen, D. Zavala-Araiza, R. Gautam, M. Omara, T. Scarpelli, J. Sheng, M. P. Sulprizio, J. Zhuang, Y. Zhang, Z. Qu, X. Lu, S. P. Hamburg, D. J. Jacob, Unravelling a large methane emission discrepancy in Mexico using satellite observations. *Remote Sensing of Environment* 260, 112461 (2021).
42. C. L. Heald, D. J. Jacob, D. B. A. Jones, P. I. Palmer, J. A. Logan, D. G. Streets, G. W. Sachse, J. C. Gille, R. N. Hoffman, T. Nehrkorn, Comparative inverse analysis of satellite (MOPITT) and aircraft (TRACE-P) observations to estimate Asian sources of carbon monoxide. *Journal of Geophysical Research: Atmospheres* 109, (2004).
43. S. Pandey, R. Gautam, S. Houweling, H. D. v. d. Gon, P. Sadavarte, T. Borsdorff, O. Hasekamp, J. Landgraf, P. Tol, T. v. Kempen, R. Hoogeveen, R. v. Hees, S. P. Hamburg, J. D. Maasackers, I. Aben, Satellite observations reveal extreme methane leakage from a natural gas well blowout. *Proceedings of the National Academy of Sciences* 116, 26376-26381 (2019).
44. D. G. Horvitz, D. J. Thompson, A Generalization of Sampling Without Replacement from a Finite Universe. *Journal of the American Statistical Association* 47, 663-685 (1952).

Acknowledgments

345 The study was supported by the National Natural Science Foundation of China (grant
346 numbers 41722101 and 41830643). The author thank J. Bastin, C. Lelong, O. Dhobb, A.
347 Rostand from Kayrros SAS for fruitful discussion.
348

349 **Author contributions:** S.P. and P.C. designed the study. C.G. performed the TROPOMI
350 inversion with help of A.A., A.B., T.L. and H.A.R.. G.L. updated PKU-CH₄ v2 inventory.
351 S.P., C.G. and G.L. performed the analysis and created all the figures. S.P. drafted the
352 manuscript. All authors contributed to commenting and writing on the draft manuscript.
353

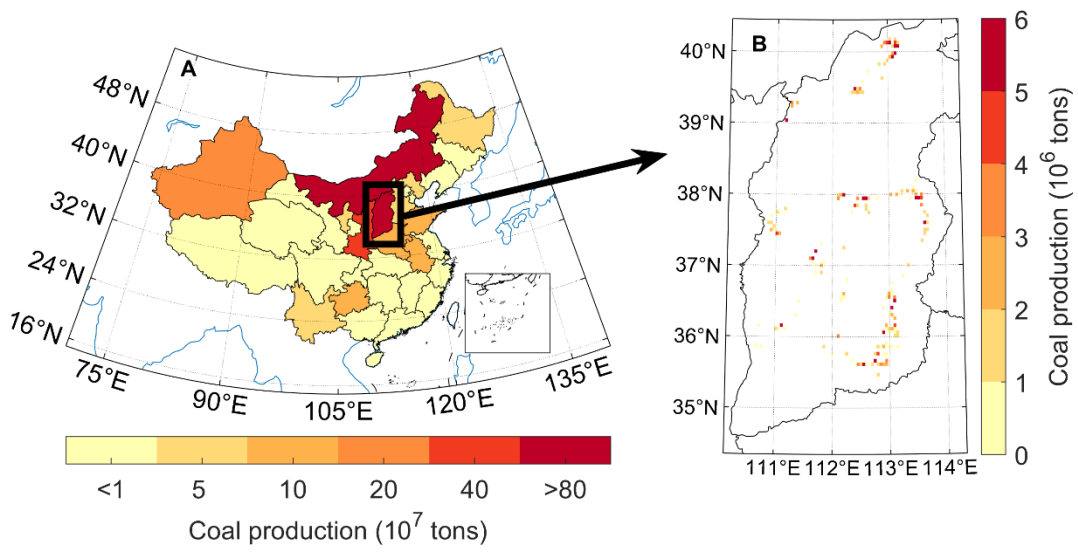
354 **Competing interests:** The authors declare no competing interests.
355

356 **Data and materials availability:** TROPOMI data (S5P L2 CH4 OFFLINE) are available from
357 the Copernicus Open Access Hub (<https://scihub.copernicus.eu/>). The meteorological
358 reanalysis data used for the forward HYSPLIT simulations are available from the Global
359 Forecast System (GFS), Environmental Modeling Center, National Centers for
360 Environmental Prediction (National Weather Service, NOAA, U.S. Department of
361 Commerce, NCEI DSI 6182, gov.noaa.ncdc:C00634); and from the Global Data
362 Assimilation System (GDAS), Environmental Modeling Center, National Centers for
363 Environmental Prediction (National Weather Service, NOAA, U.S. Department of
364 Commerce, NCEI DSI 6172, gov.noaa.ncdc:C00379). PKU-CH₄ v2 is available at
365 <https://figshare.com/s/b38a368111749f1412be>. EDGAR v6.0 is available at
366 <https://edgar.jrc.ec.europa.eu/>. GFEI v2 is available at
367 <https://doi.org/10.7910/DVN/HH4EUM>. The inversion method presented in this article is
368 constructed using the HYSPLIT model (v4.2.0; 2019), which was developed by the Air
369 Resources Laboratory at NOAA and is available from www.arl.noaa.gov/hysplit/.
370
371
372
373

374 **Figures and Tables**

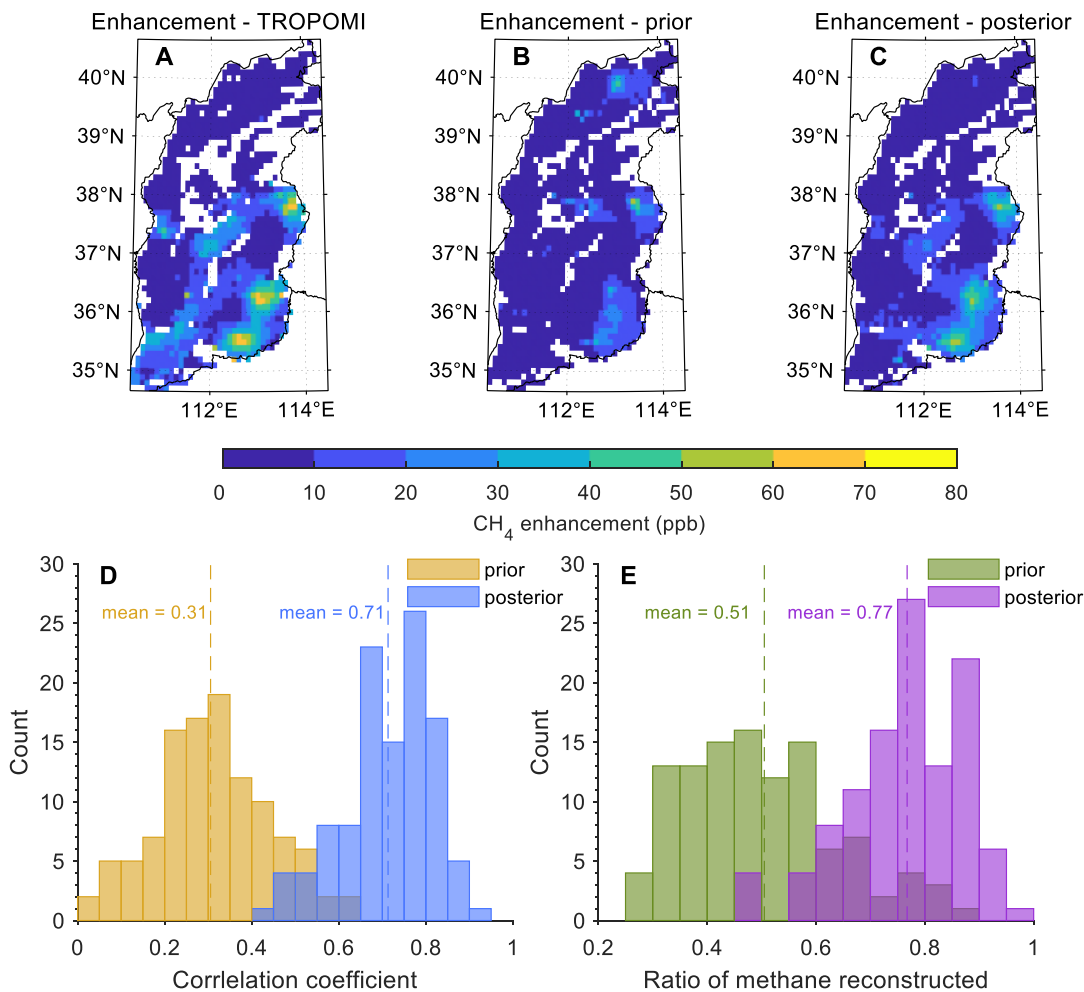
375

376 **Fig. 1. Distribution of coal production in China.** Map of the coal production at
377 province-level in 2019 over China (**A**) and distribution of gridded coal mines with
378 annual production larger than 0.6 million tons year⁻¹ with a spatial resolution of
379 0.1°×0.1° in the Shanxi Province (**B**). Note that the distribution of coal mines in
380 the Shanxi Province in (**B**) is from the ground survey dataset conducted in 2011,
381 but is scaled by the ratio of total coal production between 2011 and 2019 in the
382 Shanxi Province.

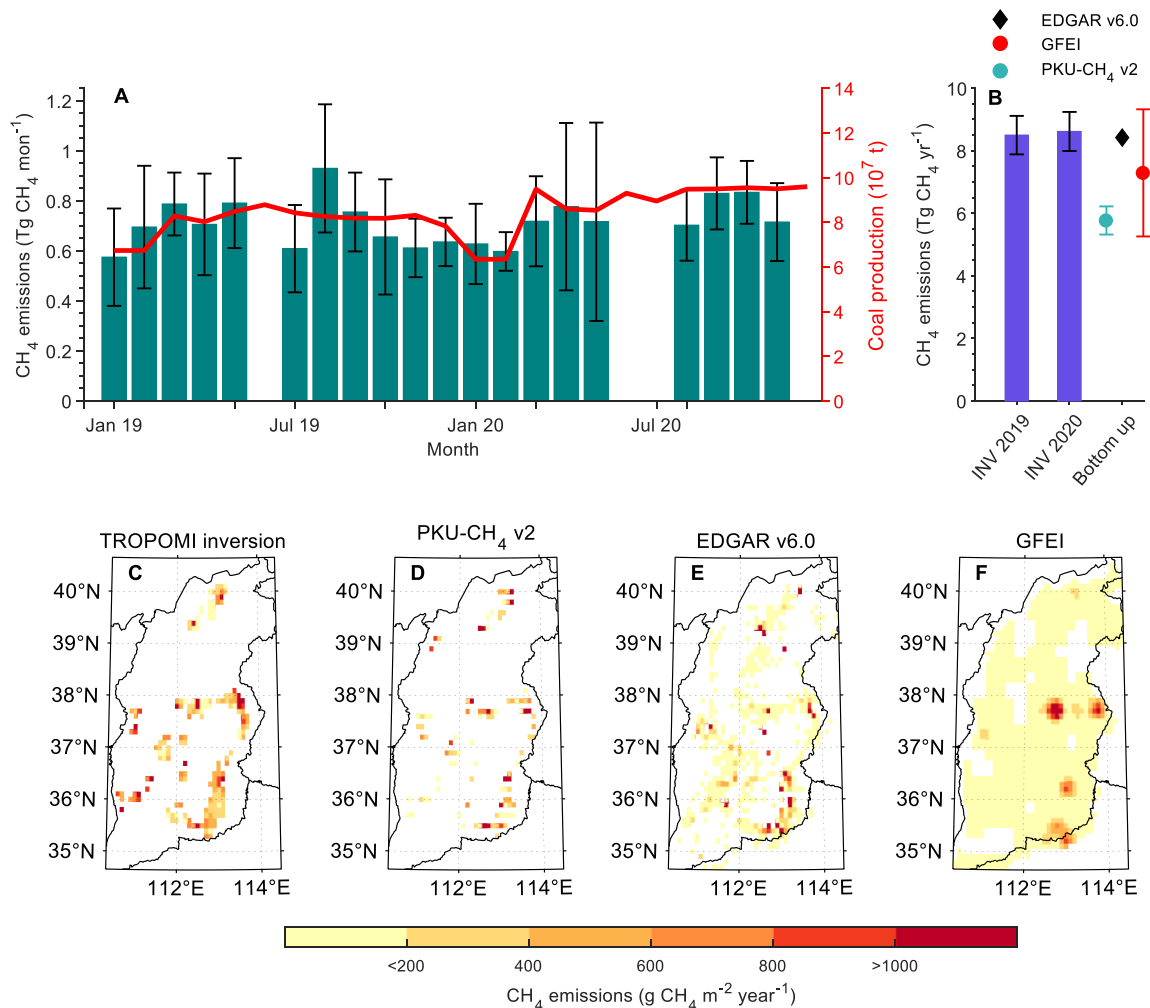


383
384

385 **Fig. 2. Spatial patterns of XCH₄ enhancement from TROPOMI, reconstructed XCH₄**
 386 **using prior and posterior emissions, with a spatial resolution of 0.1°×0.1°.** (A),
 387 averaged XCH₄ enhancement from 112 images of TROPOMI in 2019 and 2020;
 388 (B,C), reconstructed XCH₄ enhancement using prior and posterior emissions
 389 corresponding to the 112 images from TROPOMI. (D), frequency distribution of
 390 correlation coefficients between TROPOMI observations and prior (yellow) and
 391 posterior (blue) XCH₄ enhancement on an image-by-image basis. (E), frequency
 392 distribution of percentage of XCH₄ reconstructed by prior (green) and posterior
 393 (purple) estimates. Indicate figure parts with bold capital letters: (A), (B), etc.



396 **Fig. 3. CH₄ emissions from coal mining in Shanxi.** (A), monthly CH₄ emissions from
 397 coal mining from January of 2019 to December of 2020 (green bars) and coal
 398 production (red line). The total annual coal mining emissions of Shanxi province
 399 estimated from inversion by TROPOMI (INV_{TROPOMI}) and three bottom-up
 700 inventories in 2019 (PKU-CH₄ v2, EDGAR v6.0 and GFEI) are summarized in
 701 (B). The error bars show standard deviation of the inversion ensemble from
 702 INV_{TROPOMI}. Note that the data of INV_{TROPOMI} in Jun 2019, Jun 2020, Jul 2020 and
 703 Dec 2020 is missing because valid images are not enough for these months (<2)
 704 for the inversion. EDGAR v6.0 only provides the annual emission until 2018, so
 705 we scaled the coal mine emissions in 2019 by the ratio of coal production between
 706 2019 and 2018. The (C-F) panel shows the spatial pattern of CH₄ emissions from
 707 INV_{TROPOMI} and bottom-up inventories (PKU-CH₄ v2, EDGAR v6.0 and GFEI) for
 708 Shanxi in 2019.



709
710

711 **Fig. 4. Emission factor (EF) of coal mining, coal quality and depth of mining.** (A) The
 712 composition of the coal production by coal types for each prefecture in Shanxi. (B)
 713 The relationship between average maximum mining depth and the emission factor
 714 (EF) of coal methane emissions derived from TROPOMI top-down inversion
 715 ($INV_{TROPOMI}$) in Shanxi at prefecture level. Note that the color of dots in (B)
 716 corresponds to the background color in (A), with the blue denoting Jinzhong and
 717 Changzhi, the two prefectures having deeper coal seams due to crustal subsidence
 718 in three tectogenesis after coal formation in the Carboniferous-Permian (30, 31).
 719

